ADVANCED FUNCTIONAL MATERIALS
www.afm-journal.de

FULL PAPER

Inverse-Woodpile Photonic Band Gap Crystals with a Cubic Diamond-like Structure Made from Single-Crystalline Silicon

J. M. van den Broek, L. A. Woldering, R. W. Tjerkstra, F. B. Segerink, I. D. Setija, and W. L. Vos*

Three dimensional photonic band gap crystals with a cubic diamond-like symmetry are fabricated. These so-called inverse-woodpile nanostructures consist of two perpendicular sets of pores in single-crystal silicon wafers and are made by means of complementary metal oxide–semiconductor (CMOS)-compatible methods. Both sets of pores have high aspect ratios and are made by deep reactive-ion etching. The mask for the first set of pores is defined in chromium by means of deep UV scan-and-step technology. The mask for the second set of pores is patterned using an ion beam and carefully placed at an angle of 90° with an alignment precision of better than 30 nm. Crystals are made with pore radii between 135–186 nm with lattice parameters $a = 686$ and $c = 488$ nm such that $a/c = \sqrt{2}$; hence the structure is cubic. The crystals are characterized using scanning electron microscopy and X-ray diffraction. By milling away slices of crystal, the pores are analyzed in detail in both directions regarding depth, radius, tapering, shape, and alignment. Using optical reflectivity it is demonstrated that the crystals have broad reflectivity peaks in the near-infrared frequency range, which includes the telecommunication range. The strong reflectivity confirms the high quality of the photonic crystals. Furthermore the width of the reflectivity peaks agrees well with gaps in calculated photonic band structures.

1. Introduction

Photonic crystals are metamaterials with periodic variations of the dielectric function on length scales comparable to the wavelength of light. These dielectric composites are of keen interest for scientists and engineers because they offer exciting ways to manipulate photons.[1,2] Of particular interest are three-dimensional (3D) photonic crystals possessing a photonic band gap; a frequency range where no photon modes exist at all. Photonic band gap materials possess great potential to drastically change the rate of spontaneous emission and to achieve localization of light.[3–5] Control over spontaneous emission is important for many applications, such as miniature lasers,[6] light-emitting diodes,[7] and solar cells.[8,9]

Different types of 3D photonic crystals have been conceived.[10–13] Of special interest are those that potentially provide large 3D photonic band gaps. Such structures offer ultimate control of light in all three dimensions simultaneously and therefore many research groups are pursuing their fabrication.[14–20] A promising class of 3D photonic crystals has a diamond-like symmetry.[21] Among these diamond structures, inverse-woodpile photonic crystals are of particular interest[10] because of their conceptual ease of fabrication and a broad photonic band gap that is robust to disorder and fabrication imperfections.[22–24] These crystals consist of two perpendicular arrays of cylindrical pores containing air in a high-refractive-index material, see **Figure 1**A. The predicted band gap of inverse-woodpile photonic crystals has a broad relative bandwidth of more than 25%.[10,23,25] We have chosen single-crystalline silicon as a high-refractive-index material since it is conveniently available in high purity. Many techniques for the fabrication of electronical and mechanical components in silicon are available, which eases the integration of photonics and electronics with silicon.[26]

Herein we report the fabrication and characterization of inverse-woodpile photonic crystals in monocrystalline silicon. The nanostructures consist of two separate sets of pores that run in perpendicular directions; see Figure 1A for a schematic illustration. Pores run along the x (first set) and z axis (second set), and are aligned in such a way that the second pore set is centered between the pores that run in the first direction, see Figure 1B. Therefore, the resulting structure has a network

J. M. van den Broek, Dr. L. A. Woldering, Dr. R. W. Tjerkstra, Prof. W. L. Vos
Complex Photonic Systems (COPS)
MESA+ Institute for Nanotechnology
University of Twente
7500 AE Enschede, The Netherlands
E-mail: j.m.vandenbroek@utwente.nl
F. B. Segerink
Optical Sciences (OS)
MESA+ Institute for Nanotechnology
University of Twente
7500 AE Enschede, The Netherlands
Dr. I. D. Setija
ASML Netherlands B.V., 5504 DR Veldhoven, The Netherlands

DOI: 10.1002/adfm.201101101

© 2011 WILEY-VCH Verlag GmbH & Co. KGaA, Weinheim

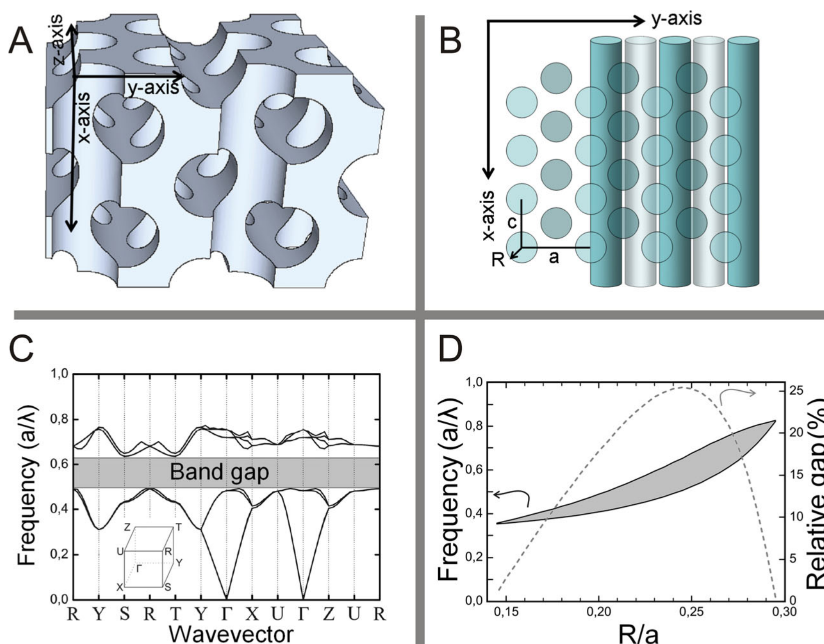

Figure 1. A) Schematic illustration of a cubic inverse-woodpile structure. The structure consists of two perpendicular pore sets parallel to the *x* and *z* axis. This perspective view shows that the pores overlap, thereby creating a topologically connected structure. B) Schematic drawing of an inverse-woodpile photonic crystal viewed along the *z* axis. Each pore set forms a centered rectangular lattice with lattice parameters $a/c = \sqrt{2}$ and Miller indices $(hkl) = (110)$. The axes of the cylinders running in the *x* direction are centered between rows of cylinders of the other set. C) Dispersion relations of light calculated for an inverse-woodpile structure consisting of a high-index material with $\varepsilon = 12.1$ (silicon) and air. The wavevector runs between high-symmetry points in the first Brillouin zone as is shown in the inset. The band gap (gray bar) of a cubic inverse-woodpile photonic crystal $[(R/a) = 0.245$ and $a/c = \sqrt{2}]$ has a broad relative bandwidth of 25.4%. D) Calculated frequency and relative band gap width versus normalized pore radius (R/a). The band gap has a maximum width of 25.4% at a central frequency $(a/\lambda) = 0.581$ for $(R/a) = 0.245$.

topology which is favorable for the desired formation of a photonic band gap.[27] The pores form a centered rectangular lattice in which the lattice parameters a and c have a ratio $a/c = \sqrt{2}$; this ensures that the 3D crystal structure is cubic with a diamond-like symmetry. Each array of pores forms an $(hkl) = (110)$ face.

By varying the relative pore radius R/a, the volume fraction of the constituent materials can be tuned and hence the photonic interaction strength. For high-index materials with a dielectric function of silicon, inverse-woodpile structures develop a band gap as shown in Figure 1C. For $(R/a) = 0.245$ the photonic band gap has a maximum width, as shown in Figure 1D. We investigate whether it is feasible to consecutively etch pores in two different, orthogonal directions in single-crystalline silicon wafers by means of complementary metal oxide–semiconductor (CMOS)-compatible methods such as reactive-ion etching.[28]

2. Fabrication of 3D Structures From 2D Structures

A scanning electron microscopy (SEM) image of a cleaved 2D silicon photonic crystal is shown in **Figure 2**A. The structure consists of the first set of pores that is etched parallel to the x axis using reactive-ion etching with a Bosch process.[29] The pores have a depth of 5550 ± 130 nm and a radius at half-depth of 159 ± 7 nm, which corresponds to a high aspect ratio of 17.5 ± 1.2. We have managed to realize nanostructures with even higher aspect ratios up to 21.6, as shown in the inset of Figure 2A. Near the top of the pores, some "scallops" appear as remnants from the Bosch process. The pores are smooth over a large depth of 5000 nm with a low tapering of 0.2 ± 0.1°, which makes these structures highly suited to optical applications such as photonic crystals. The pores are nearly identical over the extent of the 2D array, which is important to reduce unwanted light scattering.[30] Therefore, such 2D structures are excellent starting points for the fabrication of 3D inverse-woodpile crystals.

To vary the center frequency and the bandwidth of the photonic gap, it is desirable to control the pore radii of the photonic crystal.[10,25] In the present study, we aimed to make crystals with a band gap near $\lambda = 1550$ nm, which is one of the wavelengths used in telecommunication. For this we need values for $(a/\lambda) = 0.581$ and $(R/a) = 0.245$. We have managed to vary the pore radii by controlling the etching procedure, in particular the protective-step duration and capacitively coupled plasma power (CCP). By doing so, we have varied the value of R between 135 ± 7 and 186 ± 9 nm, which corresponds to $(R/a) = 0.198–0.271$, see Appendix A in the Supporting Information. This range of (R/a) was chosen because a width of the band gap of at least 50% of the maximum width is maintained, see Figure 1D.[23] As a result of this control over pore radii, the center of the band gap systematically shifts from $(a/\lambda) = 0.40–0.69$, see Figure 1D, which is a favorably large tuning range for optical applications.[31,32]

Figure 3A shows a photograph of part of a silicon wafer with 12 identical patterns in the chromium mask on the surface of the wafer. The large colorful squares are patterns with dimensions of 4.0 × 4.0 mm², which corresponds to approximately 5900 × 8300 unit cells. The squares can easily be seen by the naked eye. Since the lattice parameters are equal for each mask, the abundance of colors is caused by diffraction of different grating modes under illumination with white light.

After reactive-ion etching of the first set of pores, the chromium mask was removed. For the next fabrication step the 2D photonic crystal was cleaved along the 2D $(hk) = [10]$ direction of the crystal, which corresponds to a cleavage along the xy plane. Figure 3B shows a photograph of a cleaved piece of silicon of 10 × 20 mm² on which the blue segment of 4.0 × 2.5 mm² indicates where the pores were etched to form a 2D photonic crystal. Even though the large 2D crystal has been cleaved, it retains a large surface of some 5100 × 5900 uniform unit cells.

© 2011 WILEY-VCH Verlag GmbH & Co. KGaA, Weinheim

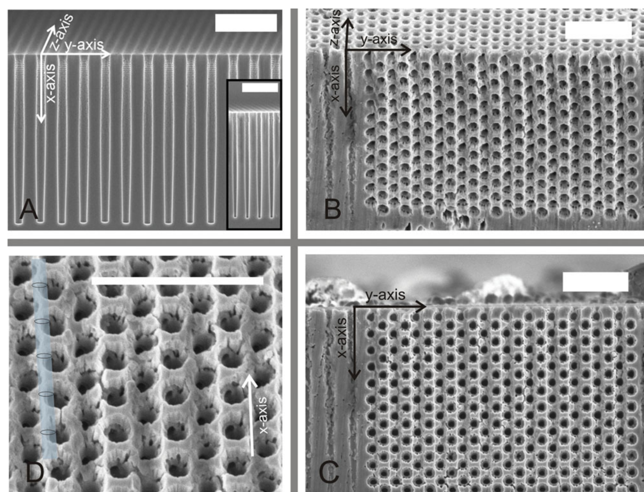

Figure 2. A) SEM image of a cross-section of a 2D photonic crystal in silicon. Smooth pores in a pattern as shown in Figure 2B are etched along the *x* axis. The depth of the pores is 5550 ± 130 nm and their radius is 159 ± 7 nm; the aspect ratio is 17.5. The inset shows etched pores with a high aspect ratio of 21.6. B) SEM image of a tilted 3D inverse-woodpile photonic band gap crystal in silicon realized by reactive-ion etching. Both the front and the top surfaces of an inverse-woodpile structure with pore radii R = 145 ± 9 nm. The 3D inverse woodpile is surrounded by the parental 2D crystal. C) The same structure tilted to show the front surface. D) Zoom-in of the (*x*–*y*) face of the inverse woodpile structure. *z*-directed pores etched perpendicular to the plane of the figure are clearly visible. The white arrow marks a place where two perpendicular pores cross each other. In all images the scale bar represents 2 µm.

To confirm that the processed wafers remain as single-crystalline silicon, we performed X-ray diffraction measurements on both an etched and a pristine wafer. The two diffraction patterns shown in **Figure 4** reveal one sharp diffraction peak at a diffraction angle of $2\theta = 69.23 \pm 0.02°$, which corresponds to the (hkl) = 400 Bragg reflection. Using Bragg's law ($n\lambda = 2d \sin\theta$) we find the atomic lattice parameter to be $d = 5.424 \pm 0.002$ Å, which is in excellent agreement with the literature.[33] From the observation of only one narrow diffraction peak, we conclude that both the silicon substrate and the silicon 2D photonic crystal are single-crystalline. Moreover, it confirms the orientation of the atomic crystal with respect to the photonic-crystal structure. An advantageous feature of our fabrication method over many previous methods that employ deposition[13,14,19] is that we realize nanostructures in crystalline silicon of high purity and high density instead of in a polycrystalline material. As a result, the density of chemical impurities in our structures is much lower, which serves to avoid spurious optical absorption. Moreover, the high index medium in our crystals is 100% densified. Thus the refractive index is maximal, which is favorable optimize the photonic interaction strength, whereas the index is lower in deposited structures.[34] Furthermore, the refractive index is well-defined, which is useful for a physical interpretation of experimental results and for the design of functional crystals.

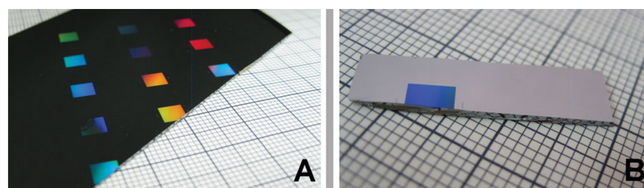

Figure 3. A) Color photograph of part of a silicon wafer containing a 50-nm chromium mask before etching. Twelve identical patterns were made in the chromium by deep UV scan-and-step lithography. The large colored areas are patterns with dimensions of 4.0 mm × 4.0 mm that show bright colors because of diffraction of different grating modes under white light illumination. B) Color photo of a large etched silicon 2D photonic crystal, cleaved to 4.0 × 2.5 mm^2, which contains approximately 5100 × 5900 unit cells. The uniform blue luster is caused by surface grating, and confirms that the high-quality crystal is uniform over its whole extent. The chromium mask has already been removed from this structure.

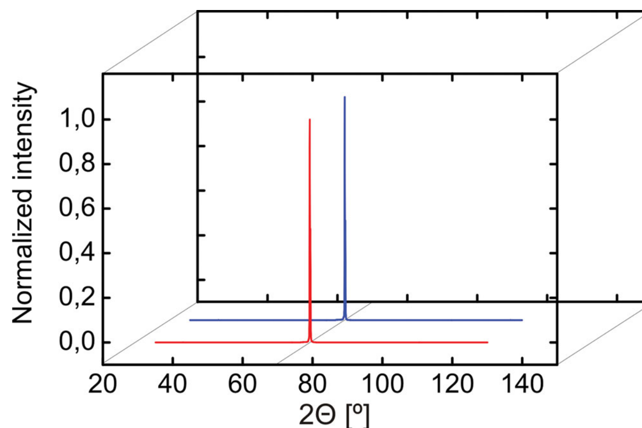

Figure 4. X-ray diffraction patterns of an etched (red) and a pristine silicon wafer (blue). Both patterns show one very sharp diffraction peak at $2\theta = 69.23°$ which is the (hkl) = (400) single-crystal Bragg diffraction peak.

After precisely aligning a second mask at 90° to a 2D array of pores[35] as shown in Figure 2A, we have managed to etch pores in the *z* direction. Thereby we realized seven individual 3D inverse-woodpile structures. An example is shown in Figure 2C, which shows the (*x*–*y*) face or (hkl) = 110 face of the inverse woodpile. On the left side of the picture we see several pores running in the *x* direction that were used to carefully align the second mask. The 3D crystal extends to over 5 × 7 µm^2, which is limited by our current mask-writing capabilities. By using e-beam or deep UV scan-and-step lithography, the areal extents of the crystal could be greatly increased. Nevertheless, the current crystal size is already sufficiently large for successful optical experiments, see Section 4.

Figure 2B shows the same crystal in an oblique perspective to show both (*y*–*z*) and (*x*–*y*) faces (110 and $1\bar{1}0$). We see that the lattice parameters and orientations of the structures in both faces are well matched. Indeed the lattice parameters for the (*x*–*y*) face are $a = 693 \pm 22$ nm and $c = 491 \pm 19$ nm, very close to those for the (*y*–*z*) face. The figure also clearly shows that all intended pores have been etched, in other words, the patterns are complete.

Figure 2D shows a zoom-in of the (*x*–*y*) face of the 3D crystal. It is clear that the second set of pores has been etched in between the first set of pores, as intended (see Figure 1A). Therefore, this result confirms our starting hypothesis that etching a second set of pores is feasible through a structure that consists of both pores and silicon; apparently, the air–silicon

© 2011 WILEY-VCH Verlag GmbH & Co. KGaA, Weinheim

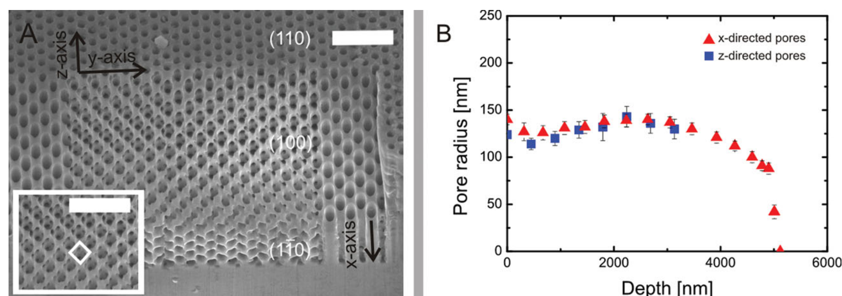

Figure 5. A) SEM of a 3D inverse-woodpile structure with pore radius R = 139 ± 8 nm and displacement Δy = 14 ± 11 nm. The 3D crystal is embedded in the large 2D crystal that was defined by the first pattern. On the right side of the figure a part of the original shape of the 2D crystal is seen. A triangular-prism-shaped part of the crystal is removed to give a view of a (100) plane in the photonic crystal. The structure that is etched in two directions possesses a surface area of 10 × 11 unit cells, with a depth of at least seven unit cells. The inset shows a magnified view of the (100) plane in a 3D inverse-woodpile structure. The white rhombic window indicates the square lattice in which the pores penetrate the (100) plane. The scale bar represents 2 μm. B) Pore radius as a function of pore depth, measured on the sample that is shown in Figure 5A. The pores running in the x direction were first etched and the second pore set was etched in the z direction. Both pore sets have the same pore radius up to a depth of 3.1 μm and thus equal tapering.

interfaces deflect the etching ions by only a small angle. We conclude that structures as shown in Figure 2 are successfully double-etched inverse-woodpile crystals.

In the ideal structure, the pores along the z axis are centered between the pores along the x axis. Positioning of the two pore sets with respect to each other introduces the possibility of unwanted structural displacements. From Figure 2B, we derive that the set of z-directed pores is displaced by only Δy = 17 ± 12 nm from the first set of x-directed pores. In the 3D structure shown in **Figure 5**A, the displacement along the y axis is only Δy = 14 ± 11 nm. For at least seven individual inverse-woodpile crystals the maximum displacement is $\Delta y <$ 30 nm, which is an excellent alignment of the two pore sets, see Appendix A in the Supporting Information. These are exciting results, since it has previously been predicted that a photonic band gap retains 90% of its width for a displacement of less than 10%, or $\Delta y \leq 69$ nm for our lattice parameters.[24] Moreover, these excellent alignments confirm that our method to pattern nanostructures on two inclined planes is indeed successful.[35]

3. Internal Structure

To investigate the detailed structure inside our inverse-woodpile crystals, we irreversibly opened several of the structures using focused-ion-beam milling, and characterized the results using SEM.[24] In this way, we investigated the dimensions of the pores as a function of depth, as well as the angular alignments of the pore sets relative to each other. Both aspects are crucial for the band gap of the photonic structure.[23]

Figure 5A shows an inverse-woodpile structure (R = 139 ± 8 nm) of which we milled away part of the crystal. To this end, we milled at an angle of 45° to both the x–y (1$\bar{1}$0) and y–z (110) faces. As a result, we obtained a (100) face of the crystal that is viewed face-on in Figure 5A. In this face, the pattern of pores is clearly square as illustrated with the rhombic window, which confirms that our 3D structures are truly cubic as intended.

One of the most challenging steps of our fabrication route is to etch the second set of pores in the macroporous 2D crystals. During this etching, the second pore set penetrates the first pore set in multiple places. Since this etching procedure is different from etching bulk silicon,[23,28] the result could give rise to a different pore radius or different pore shapes. In Figure 5B, the pore radius of both pore sets visible in Figure 5A is plotted versus the pore depth. The average radius of the first set of x-directed pores is R_1 = 139 ± 8 nm, as determined at half pore depth. The pore radius of the second set of z-directed pores is measured to a maximum depth of 3 μm as limited by the focused ion milling. The mean pore radius at a depth of 3 μm is R_2 = 134 ± 9 nm, which corresponds to an aspect ratio of >11.7. Thus, the radius of both sets are very close within ΔR = 5 nm, as was designed. Moreover, Figure 5B shows that the pore radius versus depth agrees very closely for both pore sets. This is an important result that indicates that the dimensions of the second pore set can be controlled with high precision. Another important consequence of this result is that the band-width of the photonic band gap is maintained. Previously, it was calculated that the relative width of the band gap remains more than $(\Delta\omega/\omega)$ = 20% if the pore radii differ by as much as 12 nm.[23] Therefore, we conclude that our fabrication accuracy is sufficient to maintain the broad gap.

In Figure 5B the radii of both pore sets are plotted as a function of depth. From this result we can determine the tapering of the pores, that is, how conelike a pore is instead of purely cylindrical. Tapering of the first pore set was determined between a depth of 1 μm from the bottom and 1 μm from the top. In the bottom micron there was enhanced tapering, and the upper micron was excluded due to the presence of etch scallops[29] near the top. The latter is avoided in optical applications by focusing light to the center of the pores, see Section 4. The pores show the common behavior that the pore radii slightly increase with depth, before decreasing.[29] For the first pore set, tapering is τ = 0.1 ± 0.2°. For the second pore set tapering was determined to be τ = 0.1 ± 0.2° for a depth between 1 μm from the top to a depth of 3 μm. In comparison with focused-ion-beam milling[20] the z-directed macropores etched through the macroporous silicon (Figure 5B) have much lower tapering. With ion milling we observed that the tapering of silicon and gallium phosphide yield a similar tapering to that obtained in bulk gallium phosphide was 8 ± 4°.[20] We propose that etching ions are less prone to become deflected from side walls than milling ions[24] and that the gaseous etching products are less prone to become redeposited than ion-milling debris.[20] Thus it seems reasonable that the plasma-etching process yields deeper pores with less tapering than does focused-ion-beam milling. The tapering of the pores influences the effective size of a photonic band gap.[23] It has been calculated that at τ = 0.125° tapering the band gap extends over 24.5 unit cells which

© 2011 WILEY-VCH Verlag GmbH & Co. KGaA, Weinheim

is sufficient for most nanophotonic applications, since a 20% wide gap corresponds to a minimum optical size of five cells. Therefore, in our crystal the tapering of the pores is clearly sufficiently low for band gap applications.

Apart from translational alignments, other fabrication errors will also give rise to deviations of the angular misalignments. There are three deviations from angular alignments that can occur, as summarized in Appendix A in the Supporting Information. Deviations of angular alignments may occur when the 2D crystal is not placed perpendicular with respect to the incoming ions during reactive-ion etching of the second pores. From Figure 5A we determined the α angular alignment on the (100) face for our crystal to be $\alpha << 1°$. The angles β and γ were measured on the $(1\bar{1}0)$ face of the crystal, and are equal to $\beta \leq 0.008 \pm 0.001°$ and $\gamma = 0.6 \pm 0.2°$. A relative width of the photonic band gap of more than $(\Delta\omega/\omega) = 21\%$ remains if the angular alignment of α is better than $\alpha < 5°$. For an angular alignment of β or γ better than β or $\gamma < 0.6°$, the structure remains periodic over large extents in excess of 150 lattice spacings c. Therefore, we conclude that all deviations of the angular alignments are well within the margins.[23]

4. Nanophotonic Functionality

To verify the nanophotonic functionality of our inverse woodpile crystals, we have performed reflectivity measurements perpendicular to the (x–y) face of the 3D crystal with polarized light parallel to the x axis. **Figure 6** shows the measured reflectivity versus frequency measured on an inverse-woodpile crystal with $R_1 = 186 \pm 9$ nm and $(R/a) = 0.271$. A broad reflectivity peak is observed between 6500–9000 cm^{-1} with a high reflectivity of 62% centered at 7500 cm^{-1} (or $\lambda = 1300$ nm). This broad band covers several telecommunication bands. This distinct peak was observed in the same frequency range for all polarizations over the entire 3D crystal surface.[31] The stop band corresponds to the stop gap in the Γ–Z direction (gray bar in Figure 6), which is part of the 3D photonic band gap.

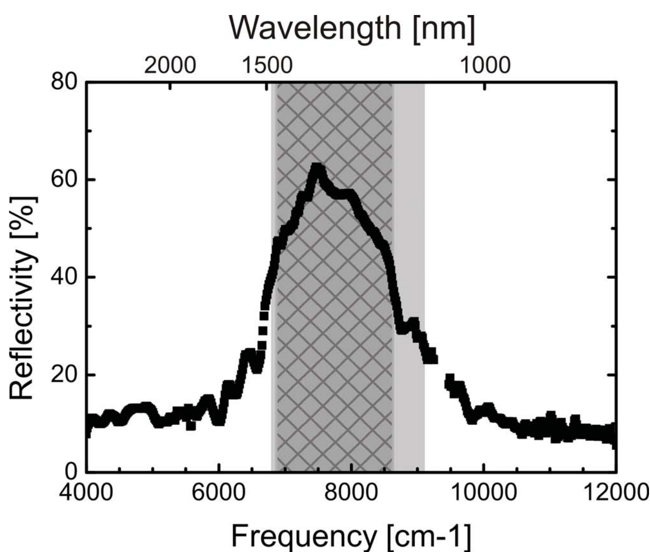

Figure 6. Optical reflectivity as function of frequency for a crystal with $R = 186 \pm 9$ nm measured on the (y–z) plane with polarized light. A strong reflectivity peak of 62% appears. The width of 2000 cm^{-1} is in very good agreement with the calculated stop gap Γ–Z direction (gray bar). The hatched bar indicates the range of the calculated 3D photonic band gap.

The maximum reflectivity is likely limited by surface roughness that scatters light in directions not collected by the objective. This assertion is supported by the observation of a lower reflectivity on crystal surfaces that were less well polished. The finite thickness of the crystals could also reduce the reflectivity. Nevertheless, peaks up to 80% have been observed on other crystals.[31] These strong peaks indicate that the crystals are sufficiently extended to show clear photonic crystal behavior. Moreover, it confirms that little light is scattered away by unavoidable deviations from perfect periodicity.[30] The peak in Figure 6 is broad with a full width at half maximum of 2000 cm^{-1}, in good agreement with the theoretical stop gap in the Γ–Z direction (gray bar). The large relative width of $(\Delta\omega/\omega) = 27\%$ confirms that the crystal interacts strongly with light. The band gap is theoretically expected between 6800 and 8670 cm^{-1} (hatched gray bar). Therefore, we conclude that our CMOS-compatible fabrication process is compatible with nanophotonic applications.

One of the main driving forces for the fabrication of photonic crystals is the realization of advanced waveguides and cavities inside the photonic crystals.[1,2,4] Therefore we briefly discuss the prospects for such functionalities in inverse-woodpile crystals. A waveguide can be made by choosing not to etch one (or more) pores in the crystal. A preliminary experiment using focused-ion-beam milling revealed a promising structure.[36] Moreover, theoretical studies have confirmed that one absent pore has waveguiding capabilities.[37] A cavity is expected to appear at the intersection of two orthogonal waveguides that each consist of an absent pore. Theoretical calculations showed that near such an intersection light is confined within a small volume of order λ^3.[38]

5. Conclusion

We have fabricated 3D photonic band gap crystals with a cubic diamond-like symmetry in a two-step process. These so-called inverse-woodpile nanostructures consist of two perpendicular sets of pores. The photonic band gap crystals were made in single-crystal silicon by using CMOS-compatible methods. Both sets of pores were made by deep reactive-ion etching and have high aspect ratios. The second set of pores etched in macroporous silicon have an aspect ratio of >11.7. The mask for the first set of pores was defined in chromium by means of deep UV scan-and-step technology. The mask for the second set of pores was also defined in chromium and carefully placed at an angle of 90° with respect to the direction of the first set of pores. The alignment precision of the second set of pores was better than 30 nm. The second mask was patterned using a focused ion beam. We characterized the crystals using scanning electron microscopy and X-ray diffraction. We have made crystals with pore radii between 135 and 186 nm, with lattice parameters $a = 686$ nm and $c = 488$ nm. By milling away slices of crystal, we analyzed the pores in both directions in detail regarding depth, radius, tapering, shape, and alignment. We demonstrate by means of optical reflectivity that our crystals have broad

© 2011 WILEY-VCH Verlag GmbH & Co. KGaA, Weinheim

reflectivity peaks in the near-infrared frequency range which includes the telecommunication range. The strong reflectivity confirms the high quality of the crystals. The widths of the reflectivity peaks agree well with the calculated photonic band structures.

6. Experimental Section

We used single-crystal silicon wafers (p-type, <100> oriented, double side polished) with a diameter of 200 mm that were coated with a 50 nm thick chromium layer. On each wafer 60 segments were patterned with deep UV step-and-scan lithography (ASML PAS5500/700).[39] The mask we used contained a pattern consisting of a centered rectangular lattice of circular pores with lattice parameters $a = 686$ nm, $c = 488$ nm, and diameter 290 nm. This pattern was chosen because of its predicted broad band gap in the near-infrared.

The patterned wafer was cleaved into pieces of approximately 2×2 cm^2. Each piece was mounted on a 100 mm p-type silicon dummy wafer and placed in a reactive-ion-etching machine (Adixen Alcatel AMS100SE). Arrays of pores were etched by an optimized reactive-ion-etching process that yields deep nanopores, as described in detail elsewhere.[29] In brief, the etching process is a deep reactive-ion etching (DRIE) process based on the Bosch protocol.[28,40] This process consists of two alternating steps, where the first step is an etching step using 62 sccm SF_6 and the second step uses 200 sccm C_4F_8 to laminate the pore walls with a polymer layer as protection. In earlier work we found that increasing the time duration of the protective step reduces the sidewall erosion.[36] The time duration of the protective step was varied between 2 and 3 s, and the duration of the etching step was 3 s. In all experiments the number of lamination and etching steps was 180. During the etching process the substrate temperature was kept at 10 °C, and the inductively coupled plasma power (ICP) was set to 1500 W. We find that increasing the capacitively coupled plasma power raises the sidewall erosion.[36] We set the CCP to 160 or 200 W (10 ms on, 90 ms off), see **Table 1**. By varying the protective-step duration and the CCP, seven different etching experiments were successfully performed.

After etching the first set of pores, the chromium mask was removed using a commercially available aqueous Cr etching solution (LSI Selectipur®). To obtain a 3D structure, a mask was placed on the cross-section of the 2D structure as described in detail elsewhere.[35] In brief, a crystal was cleaved to approximately $0.5 \times 0.5 \times 7$ mm^3, rotated by 90° and glued in slots in a silicon holder wafer using photoresist (Olin 908/35). The 2D photonic crystal and the holder wafer were coated with a 50-nm thick chromium layer using electron gun evaporation (Balzers BAK 600). The desired pattern was written in the chromium with a focused ion beam (FEI Nova 600 dual beam apparatus). In the future, the second pattern could also be written by, for instance, e-beam or deep UV step-and-scan lithography. The second mask had the same structure as the first mask. The second pattern contained typically 12×12 unit cells, and was limited by the practical settings of the ion-beam workstation. The second set of pores was etched in the same way as the first set of pores. The sample was released from the holder wafer by dissolving the photoresist with ethanol. The chromium mask was removed with chromium etch in the same way as the first mask.

To characterize the samples, we cleaved 2D samples to obtain cross-sections of the pores. The cross-sections were characterized with an SEM (LEO 1550 high-resolution) instrument. Pore depth and pore radius at half of the depth were measured. Data from up to 10 pores per image were analyzed and averaged. The top view and side view of the 3D inverse-woodpile structures were also characterized with SEM. In addition, we sacrificed a few crystals to investigate the interior. To this end, several inverse woodpile crystals were opened slice by slice by focused-ion-beam milling to analyze the internal 3D structures using SEM, similar previous reports,[24] see Appendix A in the Supporting Information. The error margins of all experiments are determined by the uncertainty in the measurements and the calibration accuracy (2% relative) of the SEM.

In these first experiments the pure processing time for one individual silicon bar containing eight equal crystals is 30 hours. For two silicon bars with different pore radii the time was 52 hours. Since the processing time per silicon bar decreases with an increasing number of samples, we feel that it would be reasonable to further reduce the processing time by making the crystals in larger batches.

Wide-angle X-ray diffraction analysis was performed on a powder diffractometer (Nonius PDS120) equipped with a CPS120 detector, using a mean wavelength of $\lambda = 1.54184$ Å from a Cu $\kappa\alpha$ generator. The X-ray beam was collimated to a spot of 0.5×0.5 mm^2 with a maximum flux of 2×10^6 counts s^{-1}. Both an etched and a pristine sample were studied to compare possible effects of the etching.

Optical-reflectivity experiments were performed with a dedicated reflectivity setup that employed a super continuum white-light source (Fianium SC-450-2) combined with a Fourier-transform spectrometer (Biorad FTS 6000). The polarized light beam was focused to a diameter of 1 μm[41] on the crystal with a 74× reflecting objective with a numerical aperture of 0.65 (Ealing). The polarization of the reflected light was analyzed. The reflectivity was calibrated by measuring reference spectra before and after the measurements with a gold mirror.

Table 1. Summary of parameter settings used for etching.

Parameter	Setting
Etching step	62 sccm 3 s SF_6
Protective step	200 sccm 2–3 s C_4F_8
CCP power	160–200 W (10 ms on, 90 ms off)
ICP power	1500 W
Total etch duration	180 cycles
Substrate temperature	10 °C

Supporting Information

Supporting Information is available from the Wiley Online Library or from the author.

Acknowledgements

The authors thank Simon Huisman and Rajesh Nair for optical experiments, Cock Harteveld for experimental help, and Merel Leistikow and Allard Mosk for discussions. This research was supported by STW/NanoNed, a nanotechnology program of the Dutch Ministry of Economic Affairs and is part of the research program of the "Stichting voor Fundamenteel Onderzoek der Materie" (FOM), which is financially supported by the "Nederlandse Organisatie voor Wetenschappelijk Onderzoek" (NWO). W.L.V. also acknowledges NWO-Vici and Smartmix Memphis.

Received: May 15, 2011
Published online:

[1] *Photonic Crystals and Light Localization in the 21st Century*, (Ed: C. M. Soukoulis), Kluwer, Amsterdam, **2001**.
[2] J. D. Joannopoulos, S. G. Johnson, J. N. Winn, R. D. Meade, *Photonic Crystals: Molding the Flow of Light*, 2nd ed., Princeton University Press, Princeton, **2008**.
[3] V. P. Bykov, *Sov. Phys. JETP* **1972**, *35*, 269.
[4] E. Yablonovitch, *Phys. Rev. Lett.* **1987**, *58*, 2059.
[5] S. John, *Phys. Rev. Lett.* **1987**, *58*, 2486.

© 2011 WILEY-VCH Verlag GmbH & Co. KGaA, Weinheim

[6] O. Painter, R. K. Lee, A. Scherer, A. Yariv, J. D. O'Brien, P. D. Dapkus, I. Kim, *Science* **1999**, *284*, 1819.
[7] H.-G. Park, S.-H. Kim, S.-H. Kwon, Y.-G. Ju, J.-K. Yang, J.-H. Baek, S.-B. Kim, Y.-H. Lee, *Science* **2004**, *305*, 1444.
[8] M. Grätzel, *Nature* **2001**, *414*, 338.
[9] A. Mihi, H. Miguez, *J. Phys. Chem. B* **2005**, *109*, 15968.
[10] K. M. Ho, C. T. Chan, C. M. Soukoulis, R. Biswas, M. Sigalas, *Solid State Commun.* **1994**, *89*, 413.
[11] C. López, *Adv. Mater.* **2003**, *15*, 1679.
[12] M. Maldovan, E. L. Thomas, *Nat. Mater.* **2004**, *3*, 593.
[13] J. F. Galisteo López, M. Ibisate, R. Sapienza, L. S. Froufe-Pérez, Á. Blanco, C. López, *Adv. Mater.* **2011**, *23*, 30.
[14] S. Y. Lin, J. G. Fleming, D. L. Hetherington, B. K. Smith, R. Biswas, K. M. Ho, M. M. Sigalas, W. Zubrzycki, S. R. Kurtz, J. Bur, *Nature* **1998**, *394*, 251.
[15] K. Wang, A. Chelnokov, S. Rowson, P. Garoche, J. M. Lourtioz, *J. Phys. D* **2000**, *33*, L119.
[16] J. Schilling, R. B. Wehrspohn, A. Birner, F. Müller, R. Hillebrand, U. Gösele, S. W. Leonard, J. P. Mondia, F. Genereux, H. M. van Driel, P. Kramper, V. Sandoghdar, K. Busch, *J. Opt. A. Pure Appl. Opt.* **2001**, *3*, S121.
[17] J. Schilling, J. White, A. Scherer, G. Stupian, R. Hillebrand, U. Gösele, *Appl. Phys. Lett.* **2005**, *86*, 011101.
[18] S. Takahashi, M. Okano, M. Imada, S. Noda, *Appl. Phys. Lett.* **2006**, *89*, 1231061.
[19] M. Hermatschweiler, A. Ledermann, G. A. Ozin, M. Wegener, G. von Freymann, *Adv. Funct. Mater.* **2007**, *17*, 2273; I. Staude, M. Thiel, S. Essig, C. Wolff, K. Busch, G. von Freymann, M. Wegener, *Opt. Lett.* **2010**, *35*, 1094.
[20] R. W. Tjerkstra, F. B. Segerink, J. J. Kelly, W. L. Vos, *J. Vac. Sci. Technol. B* **2008**, *26*, 973.
[21] K. M. Ho, C. T. Chan, C. M. Soukoulis, *Phys. Rev. Lett.* **1990**, *65*, 3152.
[22] A. Chutinan, S. Noda, *J. Opt. Am. B* **1999**, *16*, 240.
[23] L. A. Woldering, A. P. Mosk, R. W. Tjerkstra, W. L. Vos, *J. Appl. Phys.* **2009**, *105*, 093108.
[24] J. Schilling, A. Scherer, *Photonic Nanostruct. Fundam. Appl.* **2005**, *3*, 90.
[25] R. Hillebrand, S. Senz, W. Hergert, U. Gösele, *J. Appl. Phys.* **2003**, *94*, 2758.
[26] S. Roehl, A. Lin, M. Panicia, *Opt. Photon. News.* **2011**, *22*, 3, 25.
[27] E. N. Economou, M. M. Sigalas, *Phys. Rev. B* **1993**, *48*, 13434.
[28] B. Wu, A. Kumar, S. Pamarthy, *J. Appl. Phys.* **2010**, *108*, 051101.
[29] L. A. Woldering, R. W. Tjerkstra, H. V. Jansen, I. D. Setija, W. L. Vos, *Nanotechnology* **2008**, *19*, 145304.
[30] A. F. Koenderink, A. Lagendijk, W. L. Vos, *Phys. Rev. B* **2005**, *72*, 153102.
[31] S. R. Huisman, R. V. Nair, L. A. Woldering, M. D. Leistikow, A. P. Mosk, W. L. Vos, *Phys. Rev.* **2011**, *83*, 205313.
[32] M. D. Leistikow, A. P. Mosk, E. Yeganegidastgerdi, S. R. Huisman, A. Lagendijk, W. L. Vos, **2011**, Arxiv.org/abs/1106.1681.
[33] W. C. O'Mara, in *Handbook of Semiconductor Silicon Technology*, William Andrew Inc., **1990**, p. 349.
[34] J. E. G. J. Wijnhoven, L. Bechger, W. L. Vos, *Chem. Mater.* **2001**, 4486.
[35] R. W. Tjerkstra, L. A. Woldering, J. M. van den Broek, F. Roozeboom, I. D. Setija, W. L. Vos, *J. Vac. Sci. Tech. B* **2011**, in press.
[36] L. A. Woldering, Ph.D. Thesis, University of Twente, The Netherlands **2008**.
[37] H. P. Uranus, H. W. J. M. Hoekstra, W. L. Vos, presented at the 9th International Symposium on Modern Optics and Its Applications (ISMOA), Institut Teknologi Bandung, Indonesia, August **2009**.
[38] L. A. Woldering, A. P. Mosk, W. L. Vos, private communication.
[39] W. Bogaerts, R. Baets, P. Dumon, V. Wiaux, S. Beckx, D. Taillaert, B. Luyssaert, J. van Campenhout, P. Bienstman, D. van Thourhout, *J. Lightwave Technol.* **2005**, *23*, 401.
[40] F. Laermer, A. Schilp, *US Patent*, *5501893*, **1996**.
[41] G. Ctistis, A. Hartsuiker, E. van der Pol, J. Claudon, W. L. Vos, J.-M. Gérard, *Phys. Rev. B* **2010**, *82*, 195330.

© 2011 WILEY-VCH Verlag GmbH & Co. KGaA, Weinheim